Rock Mechanics and Rock Engineering (2021) 54:3873–3889
https://doi.org/10.1007/s00603-021-02481-4

ORIGINAL PAPER

Fracture Extraction from Smooth Rock Surfaces Using Depth Image Segmentation

Yudi Tang[1] · Lei He[1] · Huaiguang Xiao[1] · Ruihua Wang[1] · Wei Lu[2] · Tao Xu[1]

Received: 29 December 2020 / Accepted: 17 April 2021 / Published online: 29 April 2021

Abstract

Due to the diversity of mineral particle features in rock, including sizes, shapes, arrangements, and structural connections, the color image of the rock sample surface at laboratory scale is quite complex. Thus, unacceptable misjudgement and information loss often occur when the traditional image processing algorithms are adopted. To improve the accuracy of fracture extraction, a method based on image processing algorithms is proposed in this paper to extract fractures from 3D point clouds. First, a high-precision original depth image is generated by gridding the rock surface point cloud data with the Kriging interpolation. The hill shading method is then applied to further clarify the fractures. Finally, the fractures are extracted from depth images and compared with color images. The results show that the integrity of the fracture skeleton is significantly improved and the error rate is reduced. In combination with color images, the physical fractures and other fracture-like features can be distinguished. The proposed method provides a new idea for extracting fractures in various destructive experiments on rocks, and may be developed for recognition of discontinuities at typical engineering scale.

Keywords Image processing · Depth image · Point cloud · Rock fracture · Hill shading · Kriging interpolation

1 Introduction

Rock is a natural mineral aggregate with a certain texture structure, and it is the basic unit of rock mass (Sivakugan et al. 2013). Rocks are usually prepared into rock samples with regular shapes and smooth surfaces in the laboratory. Mechanical parameters and fracture mechanism of rock materials could be required or assessed under destructive tests, such as rock impact test (Li 2017a, b, 2019; Zou 2019), uniaxial compressive test, Brazilian split test and microwave-assisted rock breaking (Lu et al. 2020; Zhao et al. 2020; Xu et al. 2020). The accurate characterization of the fracture location, distribution, and expansion path in the rock fracturing process has a significant impact on the aforementioned research.

At the macro-level, rock is commonly regarded as a continuous, homogeneous, and isotropic medium. At the micro-level, due to the complexity and diversity of the rock formation process, different types of rocks vary considerably in texture structure, which results in a variety of intricate rock sample surface information (Xiao et al. 2020). At present, the fracture extraction is mainly through manual depiction and image processing. If the surface information of the rock sample is simple with limited loading times, the fractures could be easily determined accurately through manual depiction. However, manual depiction is time-consuming, and the accuracy and timeliness cannot be guaranteed under the following circumstances: (a) the surface information of the rock sample is complex with low contrast of fractures, (b) massive loading times or massive samples to be loaded when observing rock fracture process in real time.

Image processing is the technology for processing and analyzing digital images (IAroslavskii 2013). Though various types of image processing methods with different principles are available, the general basis is the change of the intensity and color of pixels. Four main strategies toward the automatic extraction of rock surface fractures are commonly used, including edge detection (Lemy and Hadjigeorgiou 2004; Zhu et al. 2011; Damien et al. 2019), threshold

---

✉ Lei He
helei_civil@seu.edu.cn

[1] School of Civil Engineering, Southeast University, Nanjing 210096, Jiangsu, China

[2] Faculty of Applied Science and Engineering, Department of Civil and Mineral Engineering, University of Toronto, Toronto, ON M5S1A4, Canada

segmentation (Tan et al. 2016; Otsu 1979; Talab et al. 2016; Zhang et al. 2019b), curvilinear structure enhancement (Liang 2016), and region-based segmentation (Achanta et al. 2012; Li et al. 2011). These methods can be applied to specific images with simple surface information, but limitations exist when encountering complex rock sample surfaces. To theoretically rationalize the applicability of different image processing algorithms, different types of rock samples with multiple features and complex information are selected in this paper, as shown in Fig. 1. The rock samples are 10 cm × 10 cm × 1 cm cuboid with smooth top surfaces. Their category and texture structures are shown in Table 1. Under the laboratory scale, the main features of rock sample surfaces include mineral grains, pores, original cracks, parallel banded structure, interstitial minerals, physical fractures, and the boundaries between them. The interstitial mineral is a simple classification of fracture-like textures, which could be the new mineral filling in rock fractures, or the remaining of plants and animals; original crack is the existing internal or incomplete fracturing weakness different from the physical fractures after loading. The fracture extraction by the four strategies is shown in Fig. 1.

Fractures are voids with curvilinear embedded structures caused by the disintegration and deformation of consolidated hard rocks under various stresses. Incomplete illumination cover over the fracture region results in low gray values. From the perspective of computer vision, the image features of the rock surface can be divided into two categories: the boundary and the region. Consequently, two ways are available for fracture extraction, including identification of boundary pixels between the fractures and its connected regions, and pixel extraction of the overall fracture region. Edge detection is used to extract the boundary features by identifying the pixels with evident gray level changes in the image. Since the gray level changes are obvious between the fracture region and other regions, the edge detection method could be easily applied. However, since not all the locations with obvious gray changes are the fracture boundaries, and the edge detection method is also sensitive to noise and the boundary between the non-fracture features, the detection results often show as over-segmentation. Although in recent years, various improved edge detection operators based on different principles, including the wavelet transform (Gao et al. 2019), the fuzzy theory (Wang et al. 2020), the morphology (Pei et al. 2020), and the machine learning (He and Wang 2010), have been used to optimize and classify the results of edge detection, the effects are unstable with limited applicability. Threshold segmentation is a method used to detect the regional fractures, by categorizing image pixels using thresholds setting toward gray values. The selection of the threshold plays a decisive role in the segmentation result, and the optimal threshold can be selected either manually or automatically. However, if the threshold is too large, both fractures and non-fractures would be detected; while, if the threshold is small, the fractures could be cut or even missed. Ju et al. (2018) used the Otsu method to detect the fractures of a rock sample raptured in a triaxial test with simple surface information. Zhang et al. (2019a) extracted traces in rock mass images using a hybrid algorithm which is based on global Otsu and local threshold. However, threshold segmentation is not effective for rock samples with surfaces containing different features with similar gray values. For example, in sample 1, the black mineral mica itself has a lower gray scale than the fracture, which could easily lead to misdetection. Therefore, in addition to the image gray value, Liang (2016) introduced another method of curvilinear structure enhancement to extract fractures. This method is achieved by simultaneously enhancing the curvilinear structure in the image and suppressing other shapes. Compared with threshold segmentation, the fracture curve is smoother and more concise. However, in samples 2, 3, and 4, the original cracks, parallel banded structure, and interstitial minerals similar to the physical fractures were also detected. It is inappropriate to simply group them into the same category during the fracture analysis and numerical modelling. At the same time, some fracture extraction could be missed due to low image contrast similar to low threshold segmentation. The results of region-based segmentation are all closed boundaries; hence, it can extract both boundary and regional features. The watershed method based on morphological mark is taken as an example. The area of a single segmented region is controlled by the feature scale of the selected boundary. For sample 2, the image information is simple, and the fracture positions are identified accurately with a larger feature scale. However, in other cases, since the image contains many non-fracture boundaries, over-segmentation occurs under most region-based methods (Yi et al. 2019). In summary, when there are multiple features on the surface of a rock sample, it is difficult to automatically extract fractures accurately through a certain image processing method due to the mutual interference between various features. To avoid this problem, except for the digital images, the source rock sample surface information should be expanded.

At the engineering scale, the extraction of discontinuity characteristics of rock masses from 3D point cloud data has received extensive attention. The point cloud is a massive collection of points with their spatial coordinates, and can be used to measure the surface characteristics of the target. Many scholars have used various semi-automatic methods to extract discontinuity characteristics of rock masses from raw point cloud data or digital surface models (DSM), including the methods based on curvature changes (Umili et al. 2013), three-dimensional Hough transform (Fernandes and Oliveira 2008), random sampling (Li et al. 2017a, b), region growth (Liu et al. 2019; Zhang et al. 2018) and feature clustering

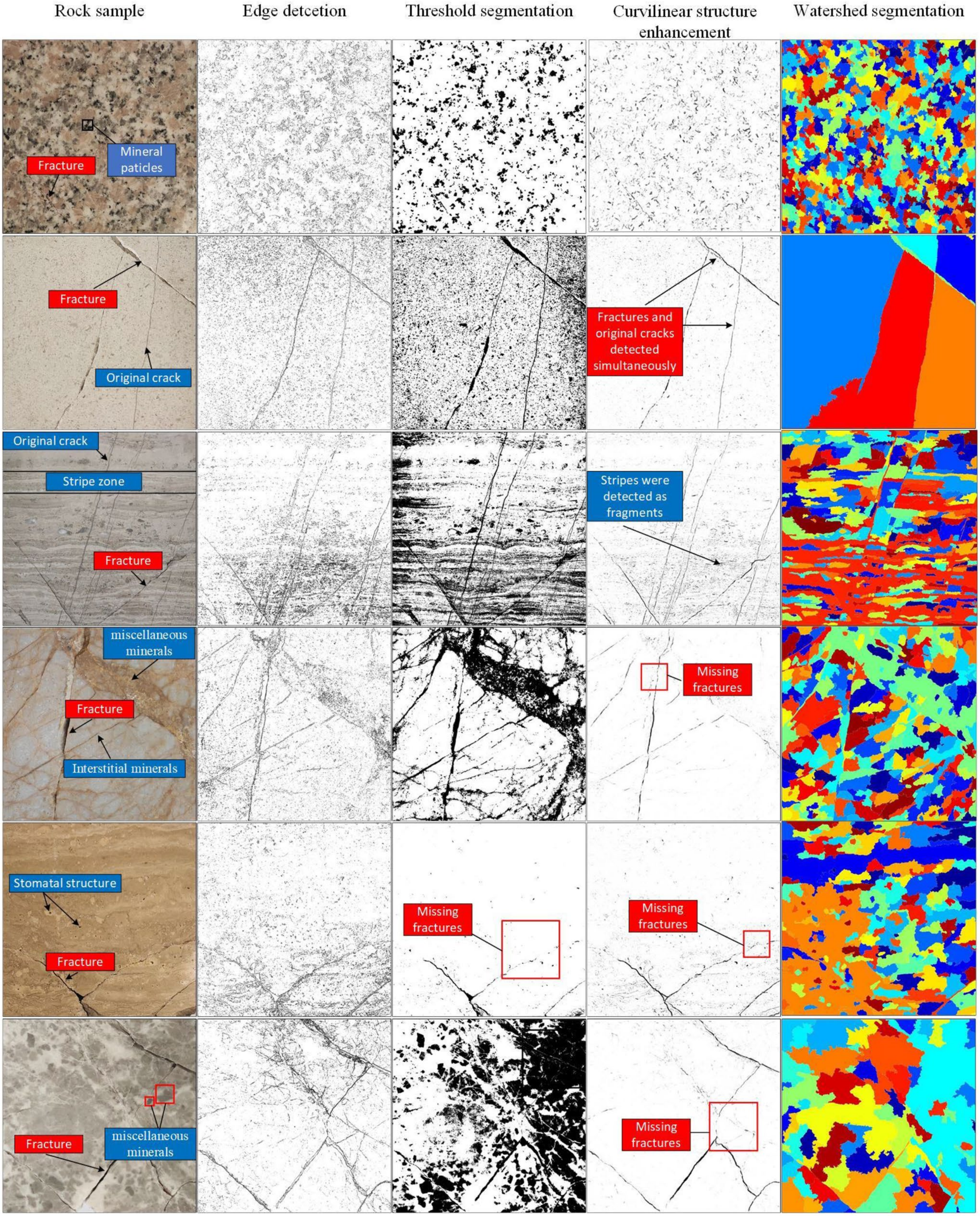

Fig. 1 Fracture extraction of rock samples (row: different rock sample cases, column: different image segmentation methods)

Table 1 The properties of rock samples

Rock sample	Name	Category	Texture structure	Feature
1	Granite	Magmatic rock (intrusive rock)	Inequigranular texture, megaphyric structure	Mineral particles
2	Marble	Metamorphic rock	Fine-grained structure blocky structure	Original cracks, mineral particles, physical fractures
3	Gabbro	Magmatic rock (intrusive rock)	Stripe structure, banded structure	Stripe zone, original cracks, physical fractures
4	Marble	Metamorphic rock	Interstitial structure, murbruk structure	Interstitial minerals miscellaneous minerals, physical fractures
5	Basalt	Magmatic rock (extruded rock)	Stripe structure, stomatal structure	Stoma, stripe structure physical fractures
6	Dolomites	Sedimentary rock	Murbruk structure	Miscellaneous minerals physical fractures

(Wang et al. 2019). Inspired by this, the three-dimensional point cloud information is considered for fracture extraction of rock samples under laboratory scale. Limited studies in this area are currently available, which may be due to the difficulty in extracting the curvilinear embedded structure, though it is effective for collecting the discontinuous characteristics exposed (Zhang et al. 2019). Xu et al. (2020) proposed a new fast fuzzy clustering method based on photogrammetry, to extract the discontinuities on the rock surface. This method is effective for not only planar but also curvilinear structures, while more than 5 features should be manually selected. It also reflects another shortcoming of the current extraction method based on the point cloud data: in the process of pre-processing and discontinuity extraction, various commercial software will inevitably being used with heavy workload, whose operations and accuracy would be subjectively affected by the non-automation process.

Compared with the point cloud data, pixel-based image processing algorithms are more mature and better developed, with advantages in the identification of topological characteristics and automation process. The accuracy of fracture extraction could be significantly improved, if the three-dimensional information of rock samples can be converted into image data for processing. In fact, with the development of stereo vision technology and the emergence of hardware devices, such as the depth camera that describes the three-dimensional information of the scene, the integration of depth images and traditional color images is better explored recently, to improve the image segmentation and feature extraction. The depth image is an image with the pixel value being the distance from the image collector to each point in the scene. Similar to the point cloud data, it can directly reflect the geometric features of the object. A lot of related research is based on several data sets whose main contents are indoor scenes and daily objects, such as NYU2 (Silberman et al. 2012), RGBD (Lempitsky et al. 2009), B3DO (Janoch et al. 2011), SUN3D (Xiao et al. 2013) data sets. It is preliminarily proven that the RGB-D image segmentation that integrates the depth and color images is better than the color image segmentation only (Cong et al. 2020). Galdames et al. (2017) extracted features from different types of depth and color images of rock blocks, and used SVM to accurately classify the rock blocks of different lithologies. On this basis, the accuracy of classification was further improved by applying hyperspectral images (Galdames et al. 2019). From the literature review, only these two studies were found on the depth images for the feature extraction of rock surface.

This study aims to improve the accuracy of fracture extraction of rock surfaces by applying depth images into the image processing technology. Due to the low resolution of depth images obtained by current sensors, it cannot meet the requirements of an exact description of undulating rock surface. Thus, the pre-processing of point cloud, data gridding, and hill shading are operated to generate depth images. Besides, the depth image and the color image are registered by properly cutting and modifying the size of images. Finally, according to the characteristics of the depth image and the color image, suitable image processing algorithms are selected and applied to obtain specific fracture extractions, and the results can be integrated when necessary.

2 Materials and Methodology

2.1 Rock Samples and Data Collection

The six rock samples shown in Fig. 1 are prepared from 5 different types of rocks, including granite, marble, gabbro, basalt, and dolomite. They have different rock texture structures, image color and gray values, and fracture distributions. The rock samples are 10 cm × 10 cm × 1 cm cuboids with smooth top surfaces, and the fractures are resulted from vibration and hammering. The point cloud data of the rock sample are obtained by the 3D Systems Capture handheld scanner. Point cloud can be promptly obtained by connecting to a laptop through a twisted pair cable, as shown in Fig. 2. 985,000 points can be

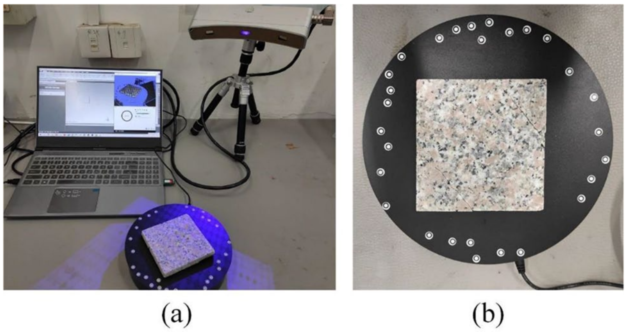
(a) (b)

Fig. 2 Schematic diagram of 3D Systems Capture work, **a** configuration of the 3D laser scanning system, **b** close-up of the turntable and rock sample

captured in 0.3 s per scan, with a positioning accuracy of 0.110 mm/300 mm, and a field of view of 124 × 120 mm (near) and 190 × 175 mm (far). As for scanning, the rock sample is placed on the electric turntable. The turntable rotates 45° every time until a full-circle rotation is reached. The white positioning points in the turntable are used for point cloud splicing of different angle scans, and subsequently for the registration of color images and depth images. In particular, for rock samples with dark surfaces, the structure light will be absorbed, and a three-dimensional scanner developer should be applied before scanning. Each scanned point cloud model contains approximately 360,000 points. Take rock sample 6 as an example, Fig. 3. illustrates the four steps of fracture extraction from point cloud data: (1) Pre-processing of point cloud; (2)

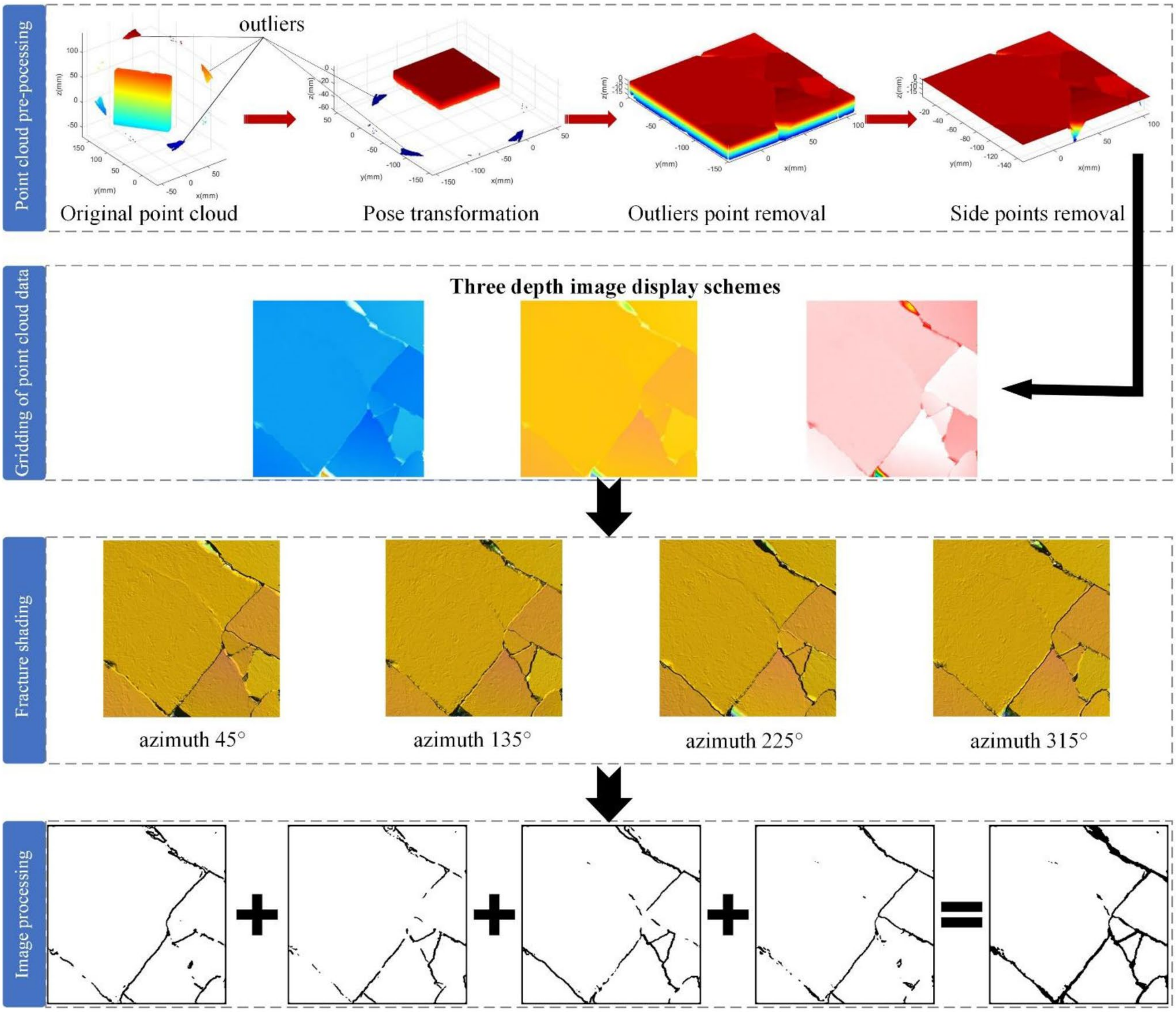

Fig. 3 Flow chart of fracture extraction from rock surface

Gridding of disordered point cloud data; (3) Fracture shading; and (4) Processing of depth image.

2.2 Generation of Depth Images from Point Clouds

The initial point cloud model contains the overall geometric information of the rock block, while the pixel value of a depth image only depends on the distance from the target surface point to the depth sensor plane. In this study, the top surface of the rock sample is taken as the target surface. The x–y plane of the global coordinate system is used as the depth sensor plane. After adjusting the target surface to be parallel to the x–y plane, the z coordinate of the top surface point is the distance required to generate a depth image.

The pose of the rock sample is controlled by 6° of freedom, that is, the three degrees of freedom of movements along the three rectangular axes of x, y, and z, as well as the 3° of freedom of rotation around these axes. In the point cloud global coordinate system, the three degrees of rotational freedom are the roll angles around the x axis, the pitch angle around the y axis, and the yaw angle around the z axis. To make the target surface parallel to the x–y plane, only the rotational freedom needs to be calculated. For two three-dimensional points P_1 $(x_1, y_{1,} z_1)$ and P_2 (x_2, y_2, z_2), the transformation from the point P_1 to P_2 through the rotation matrix R can be expressed as:

$$P_2 = R \times P_1. \tag{1}$$

The rotation matrix R can be determined by the yaw angle, pitch angle, and roll angle, which rotating around z, y, and x axes in order. The formula is shown as follows (Javed 2020):

$$R_x = \begin{bmatrix} 1 & 0 & 0 \\ 0 & \cos(\text{roll}) & -\sin(\text{roll}) \\ 0 & \sin(\text{roll}) & \cos(\text{roll}) \end{bmatrix}, \tag{2}$$

$$R_y = \begin{bmatrix} \cos(\text{pitch}) & 0 & \sin(\text{pitch}) \\ 0 & 1 & 0 \\ -\sin(\text{pitch}) & 0 & \cos(\text{pitch}) \end{bmatrix}, \tag{3}$$

$$R_z = \begin{bmatrix} \cos(\text{yaw}) & -\sin(\text{yaw}) & 0 \\ \sin(\text{yaw}) & \cos(\text{yaw}) & 0 \\ 0 & 0 & 1 \end{bmatrix}, \tag{4}$$

$$R = R_x \times R_y \times R_z. \tag{5}$$

Among them, R_x, R_y and R_z are the rotation matrices around the x, y, and z axes, respectively.

Next, the least square method is applied to fit a plane to the target surface and find the normal vector $\boldsymbol{n}$ of the plane. The transformation R, that rotates the vector $\boldsymbol{n}$ to coincide with the normal vector of the x–y plane, is the rotational matrix that could adjust the upper surface of the rock model to be parallel to the x–y plane. For this transformation, the yaw angle is 0 degrees; the pitch angle is the angle between the z axis and the projection of the vector $\boldsymbol{n}$ on the x–z plane; and the roll angle is the angle between the z axis and the projection of $\boldsymbol{n}$ on the y–z plane. The analogic operation can convert the side of the rock sample to be parallel to the corresponding coordinate plane (x–z and y–z plane). In addition to the pose transformation, the pre-processing of the point cloud includes another two steps: the removal of the outliers and side points.

Compared with the randomness among point clouds, that is, the lack of order and arranged relationships between points, the pixels of the digital image are arranged in order and a certain relationship exists between adjacent pixels. Therefore, point cloud gridding is an indispensable step in the generation of depth images. In this paper, a data gridding method based on kriging interpolation is adopted to objectively estimate the unknowns of the regionalized variables. The ordinary Kriging interpolation is a method based on the theory of variogram, which can compare the original data and the semi-variance function. It assumes the space attribute z is uniform, and the same mathematical process is applied for any point (x, y) in the space. The interpolation formula is shown below (Matheron 1963):

$$\hat{z}_0(x_0, y_0) = \sum_{k=1}^{N} \lambda_k z(x_k, y_k). \tag{6}$$

Among them, (x_0,y_0) is the estimated value of the point (x_0, y_0); N is the number of points in the sample; λ_k is the Kriging weight coefficient; $z(x_k, y_k)$ is the true value of the point (x_k, y_k). For a circular neighborhood with a radius of r at the point (x_0, y_0), divide it into 4 sectors with two mutually perpendicular diameters, then set the most and least sampling points that can be used in the neighbourhood and in each sector separately. For the rock surface data in this paper, circular neighborhood with a radius of 0.07 is used, in which the maximum number of sampling points in the entire neighborhood is 64, and the maximum and minimum sampling points of each sector are 16 and 8, respectively.

Compared with the traditional interpolation methods, the Kriging method not only considers the numerical value of the object in the process of data gridding, but also considers the spatial correlation of the described object, which makes the interpolation result more scientific and closer to the actual situation. This technique is suitable for any surface interpolation with point data. The original depth image of the rock sample could be obtained with the grid data displayed as a cloud image. Inconsistent color schemes have a slight impact on subsequent fracture extraction and the resolution of the depth image is 3000×3000 pixels, as shown in Fig. 3.

2.3 Fracture Enhancement

2.3.1 Hill Shading

The fracture morphology features in the original depth image are not evident, and it is difficult to directly extract the fractures with image processing algorithms. Hill shading is a method to highlight the undulations, distribution, and morphological characteristics of the landform through the contrast generated by light irradiation. It is usually used in the display of landforms on large-scale maps. By taking the undulation of the rock sample surface as a small-scale landform, hill shading can be applied to significantly enhance the fracture characteristics in the depth image.

Illumination is an important factor indicating the effect of the hill shading generation and the Phong illumination model is the most commonly used model for hill shading. It is assumed that the light source is a point light source, and the reflection of objects is subdivided into diffuse reflection and specular reflection. The mutual reflection between objects is not considered, and only a constant is used to approximate the ambient light. The light intensity can be calculated from the following shading function (Hu et al. 2011):

$$I = I_{\mathrm{pa}} k_{\mathrm{a}} + I_l (k_d \cos i + k_s \cos^n \gamma), \tag{7}$$

where I_{pa} is the ambient light intensity of the object ($0 \le I_{pa} \le 1$); k_a is the ambient light reflection coefficient of the object surface ($0 \le k_a \le 1$); I_l is the light intensity of the incident light ($0 \le \mathrm{I}_1 \le 1$); k_d is the diffuse reflection coefficient ($0 \le k_d \le 1$); and i is the light source incident angle; k_s is the specular reflection coefficient ($0 \le k_s \le 1$); n is the surface glossiness; and γ is the angle between the specular reflection direction and the line of sight. For color images, the shading function is used to calculate each component of the three primary colors. The color lighting model is as follows:

$$\begin{aligned} I_r &= I_{par} k_{ar} + I_{lr} (k_{dr} \cos i + k_{sr} \cos^n \gamma) \\ I_g &= I_{pag} k_{ag} + I_{\mathrm{lg}} (k_{dg} \cos i + k_{sg} \cos^n \gamma) \\ I_b &= I_{pab} k_{ab} + I_{lb} (k_{db} \cos i + k_{sb} \cos^n \gamma) \end{aligned} \tag{8}$$

Among them, the meaning of the parameters is similar to Eq. (7), which are the components of R, G and B channels. Since too high or too low light intensity will make the image too bright or too dark, resulting in low image contrast between fractures and background, in this paper, the ambient light intensity I_{pa} and the incident light intensity I_1 are both set to 0.1 based on tests. The reflection coefficient of rock surface is generally between 0.3 and 0.6. To automate and simplify the shading process, k_{a}, k_{d} and k_{s} are all set as 0.5. The value for surface glossiness n is related to surface smoothness. For smooth surfaces like metal and glass, it is generally more than 100, and for rough surfaces like paper, wood and chalk, it is generally a number between 0 and 1. For the polished smooth rock samples, the value $n = 100$ is selected.

Most of the parameters in the illumination model are constant, while the light source incident angle i is affected by the depth value of the grid data. The process of hill shading can be described as two steps. First, the grid data of the sample surface are divided into micro-units; second, the normal vector $\boldsymbol{p}$ of each micro-unit can be represented by vectors $\boldsymbol{a}$ and $\boldsymbol{b}$ along with axes x and y (Yang et al. 2017):

$$\vec{a} = \begin{bmatrix} a_x \\ a_y \\ a_z \end{bmatrix} = \begin{bmatrix} C_1 \\ 0 \\ \frac{[(D_4 - D_1) + (D_3 - D_2)}{2} \end{bmatrix}, \vec{b} = \begin{bmatrix} b_x \\ b_y \\ b_z \end{bmatrix} = \begin{bmatrix} 0 \\ C_2 \\ \frac{[(D_2 - D_1) + (D_3 - D_4)}{2} \end{bmatrix} \tag{9}$$

$$\vec{p} = \vec{a} \times \vec{b} \tag{10}$$

sAmong them, D_1, D_2, D_3 and D_4 are the depth values corresponding to the four corner points of the micro-unit; C_1 and C_2 are constants. The shading results are more natural and smooth while the calculation costs more time as the size of the micro-units become smaller. In this paper, a set of 3×3 pixels is selected as the micro-unit.

Then, to determine its gray value, the illuminance of each unit is calculated according to the relationship between the unit plane and the incident light. As shown in Fig. 4, the oblique parallel light $\boldsymbol{S}$ is irradiated on the x–y plane at an altitude angle θ. $\boldsymbol{OS'}$ is the projection of $\boldsymbol{OS}$ on the x–y plane. The angle between $\boldsymbol{OS'}$ and the true north in clockwise is the azimuth α. $\boldsymbol{ON}$ is the normal vector of the plane, and the angle between the normal $\boldsymbol{ON}$ and the light

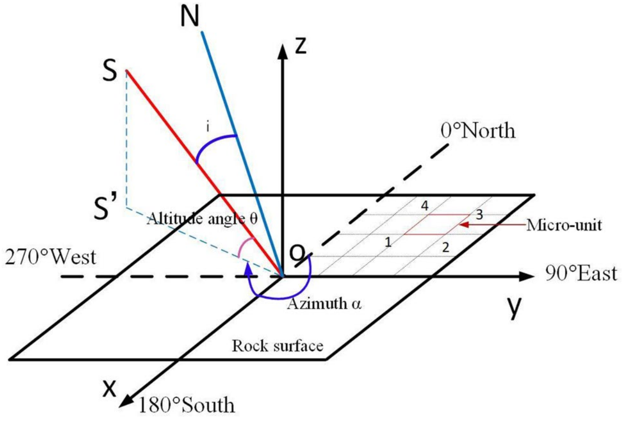

Fig. 4 The geometric principle of the shading method

OS is i. Then, the components of the vector $\boldsymbol{S}$ in the three axial directions can be expressed as follows:

$$S_x = -\cos\theta \cdot \cos\alpha$$
$$S_y = \cos\theta \cdot \sin\alpha \tag{11}$$
$$S_z = \sin\theta.$$

In addition, the incident angle i of the light source satisfies the following relationship:

$$\cos i = \frac{S_x(a_y b_z - a_z b_y) + S_y(a_z b_x - a_x b_z) + S_z(a_x b_y - a_y b_x)}{\sqrt{(a_y b_z - a_z b_y)^2 + (a_z b_x - a_x b_z)^2 + (a_x b_y - a_y b_x)^2}}. \tag{12}$$

Substituting the above relations into the illumination model for calculation, the illuminance of the surface micro-unit under a certain illumination can be obtained. The illuminance is converted to grayscale, afterwards, the halo rendering is established according to the principle of illumination and shadow.

2.3.2 Selection of Azimuth and Altitude Angle

The shading effect of fractures directly determines the accuracy of fracture extraction. In the shading method, the two essential inputs are the azimuth and the altitude angle of the parallel light. When the parallel light irradiates from the tangential direction at the altitude angle θ and the azimuth α, the blind region of the parallel light exists which contains the fracture exceeding half of the actual fracture width L, and the shading width of the fracture is L_1; When the parallel light is irradiated from the tangential direction at the altitude angle θ and the azimuth $\alpha + 180°$ instead, the blind region of the parallel light contains the fracture that exceeds half of the actual fracture width L from the opposite direction, and the shading width of the fracture is L_2. When the sum of L_1 and L_2 is greater than L, the fracture is completely shading, as shown in Fig. 5b. Moreover,

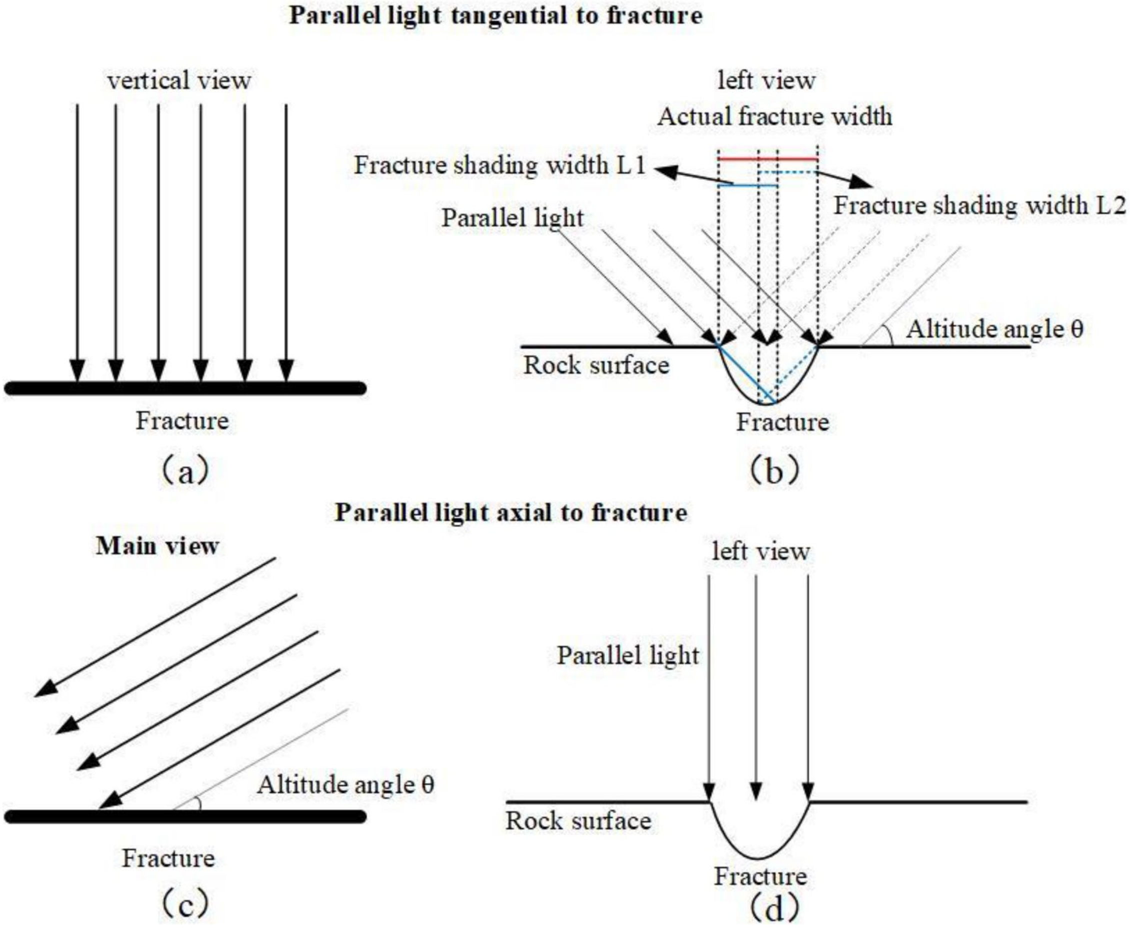

Fig. 5 Schematic diagram of the fracture under tangential and axial parallel light irradiation, **a**, **b** parallel light tangential to the fracture, **c**, **d** parallel light axial to the fracture

when the parallel light is irradiated on the fracture axially, the entire fracture is illuminated and no shadow presents. Therefore, the optimal fracture azimuth is the two opposite tangential directions of the fracture. As shown in Fig. 6, the shading images of the fracture in the red region are illustrated with an azimuth of 45° and 225°, respectively. However, it can be found that the shading effect of the fracture at 225° is much better than that at 45°, because there is a height difference on both sides of the fracture.

Under the influence of inhomogeneous stresses or the inhomogeneity of the rock sample itself, the displacement of both sides of the fracture differs during the fracturing process. The existence of the height difference affects the shading effect of the fractures. As shown in Fig. 7a, the height

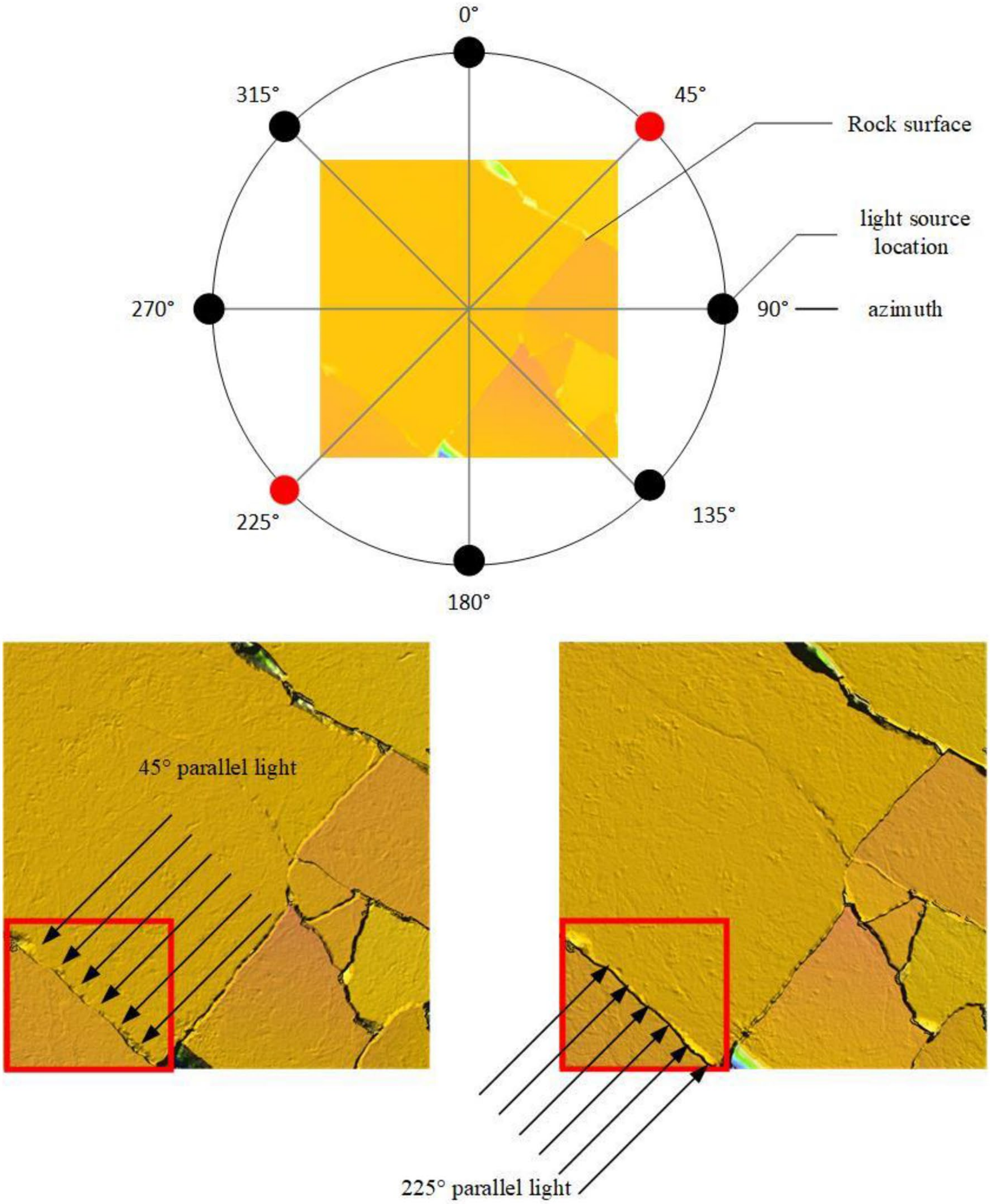

Fig. 6 Shading image of sample 6 at an azimuth of 45° and 225°

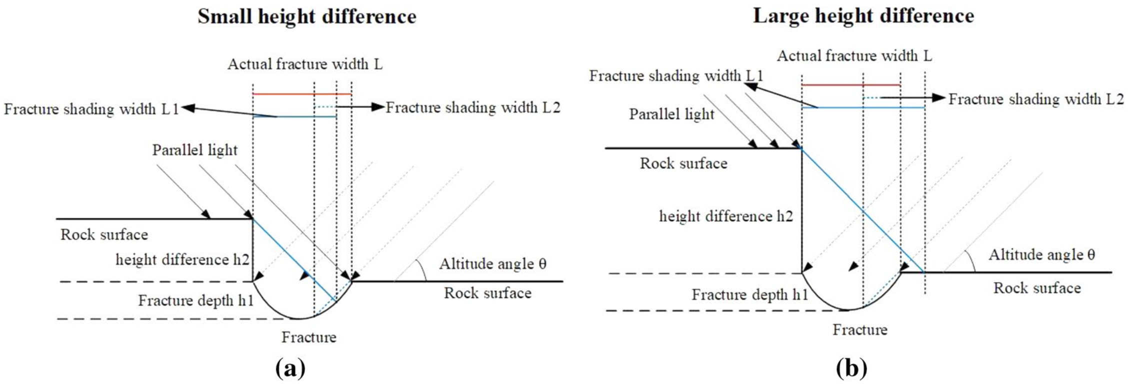

Fig. 7 Schematic diagram of shading fractures with height difference, **a** small height difference, **b** large height difference

difference on both sides of the fracture is small, and the shading effect of the fracture is similar to that of no height difference. However, it can be seen that if the altitude angle θ keeps increasing, the sum of the lengths of L_1 and L_2 will be less than L, and at the same time, the fracture will split into two parallel fractures; In Fig. 7b, the height difference between the two sides of the fracture is large, and the entire fracture is located in the blind area of the left of parallel light. At this time, the fracture is enlarged, and a certain degree of misdetection in the fracture would be indicated, which is also shown in Fig. 6. Therefore, the selection of the altitude angle θ for shading should be manually performed and examined to satisfy the following geometric relationships:

$$arc\cot\left(\frac{L}{2(h_1+h_2)}\right) \le \theta \le \operatorname{arccot}\left(\frac{L}{h_2}\right). \tag{13}$$

Among them, h_1 is the depth of the fracture, and h_2 is the height difference on both sides of the fracture.

2.4 Depth Image Processing

The first three rows of images in Fig. 8 show different color schemes for the depth image after shading. The bimodal features are obvious in the three histograms. The first peak is relatively low, which is the gathering region of fracture pixels; the second peak is higher, which is the gathering region of smooth features on the rock sample surface. As the gray histogram of the color image has only one peak which indicates that the fracture pixels are scattered in a considerable dynamic range, it is difficult to extract fractures completely and noiselessly by the threshold segmentation method.

According to the two-mode histogram method (Qian and Huang 1996), if the image gray histogram is double-peaked, the lowest point between the double peaks is selected as the threshold for image segmentation. In addition, the depth image generated by this method has two other features:(1) Large amounts of salt and pepper noise exists in the image;(2) The depth images generated under each azimuth have their own advantages and disadvantages for the expression of different fractures. Therefore, the fracture extraction algorithm of the depth image should include the following two main steps:

(a) Iterative median filtering. Since the surface of the rock sample cannot be flawless, and the subtle convex and concave structures can be identified by hand-held point cloud scanning, the depth image has salt and pepper noise on it. Median filtering is a nonlinear signal processing technology that can effectively suppress noise based on the ranking statistical theory. The basic principle of median filtering is to replace the value of a point in a digital image with the median value of its neighbourhood, so that the surrounding pixel values are close to the true value, thereby eliminating isolated noise points (Wang 1992; Kumar and Sodhi 2020). To achieve zero noise in the binarized depth image, iterative median filtering is performed on the image in this study. The termination condition of the iteration is: all the pixel values in the image no longer change when median filtering is performed.

(b) Fusion of depth image binarization results under different azimuths. Any single shading image under a certain azimuth for fracture extraction will cause incomplete extraction and any fracture must be clearly portrayed under a certain azimuth. This example performs unified image segmentation on the depth images under four azimuths (45°, 135°, 225° and 315°), superimposes four binarized images, and uses closing operations and filling holes to obtain the final depth image. The fracture extraction results are shown in Fig. 3. This operation can ensure no fracture lost with iterative median filtering.

Fig. 8 Gray histogram of the rock sample (the first three rows are the grayscale histograms of different depth image color schemes, the fourth row is the grayscale histogram of the color image)

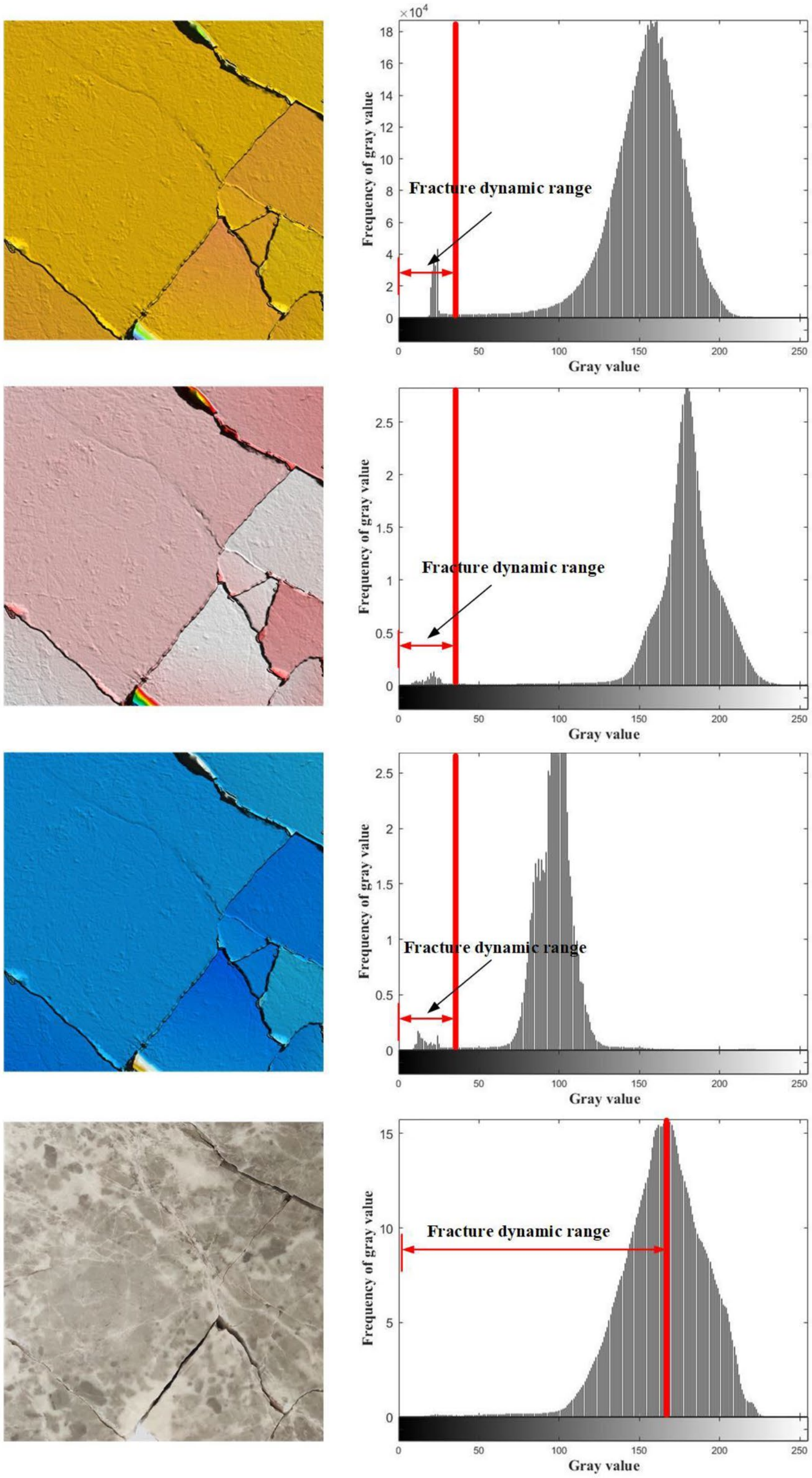

3 Results

To quantitatively discuss the accuracy of fracture extraction in color images and depth images, all the recognition results are converted from binary images to fracture skeletons through image thinning algorithms, as shown in Fig. 9. The entire process from the rock sample to the fracture skeleton by the proposed method takes about 1 min. The rock surface truth is obtained by hand-drawing. The physical fractures and the fracture-like curvilinear structures are indicated in

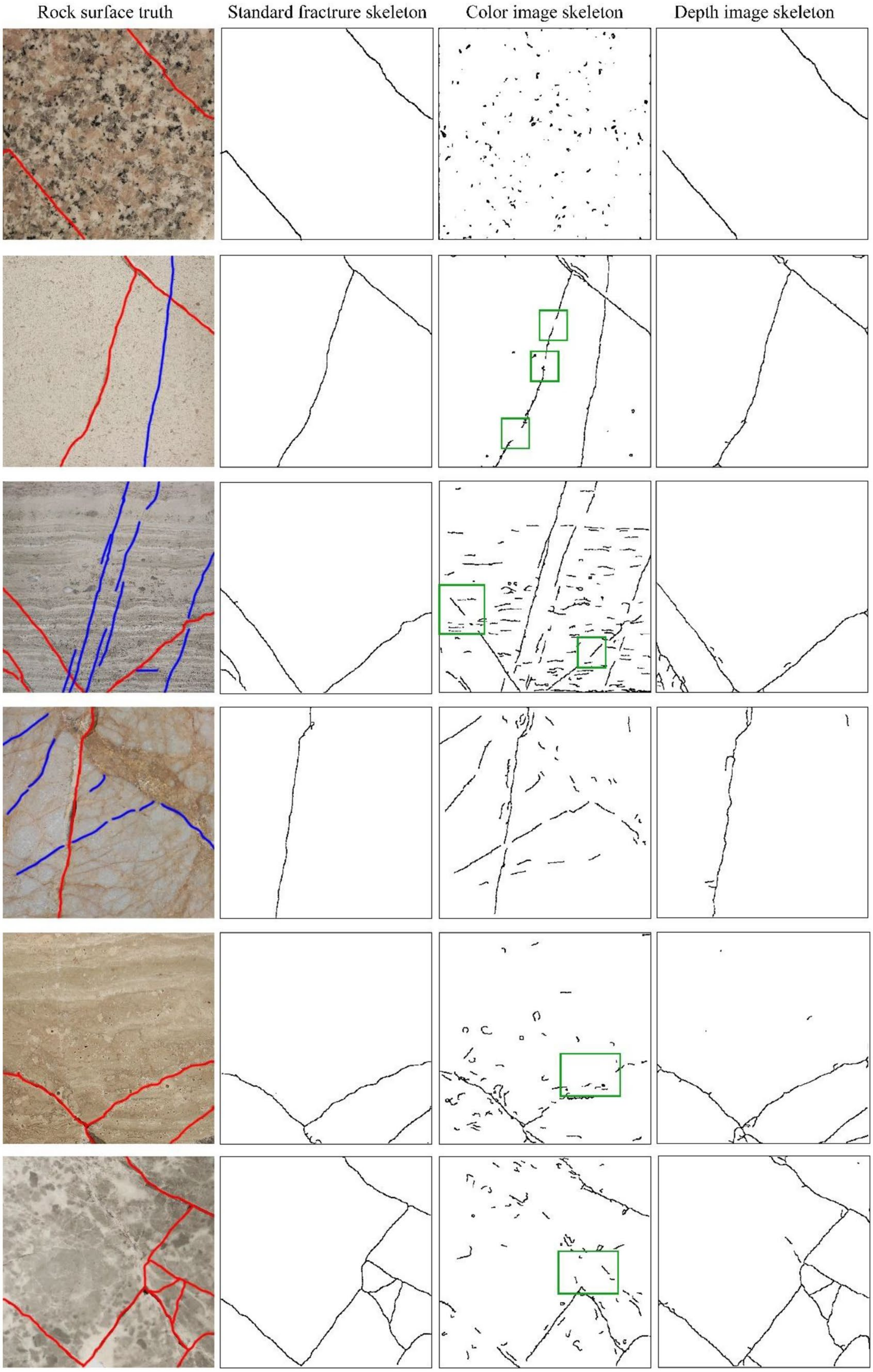
Rock surface truth
Standard fractrure skeleton
Color image skeleton
Depth image skeleton

◂**Fig. 9** Extraction results of fracture skeleton (the red marks are physical fractures, the blue marks are fracture-like structures, the green marks are missing detections in color image results)

red and blue, respectively. The standard fracture skeleton is obtained by skeletonizing the red physical fractures of the rock surface truth. The extraction algorithm of the color images will be introduced in Sect. 3.3.

3.1 Quantitative Evaluation Index of Fracture Skeleton

Three quantitative parameters are proposed: the positive detection rate *PDR*, the error rate *ER*, and the missed detection rate *MR* of the fracture skeleton. The formulas are expressed as follows:

$$\mathrm{PDR} = \frac{N_p}{N_r}, \tag{14}$$

$$\mathrm{ER} = \frac{N_e}{N_r}, \tag{15}$$

$$\mathrm{MR} = \frac{N_m}{N_r}. \tag{16}$$

Among them, N_p represents the positive detection pixels, which is defined as the number of pixels in the skeleton to be evaluated that match the standard fracture skeleton. N_e is the number of error pixels, N_m is the number of missed detection pixels, N_r is the total number of pixels of the standard fracture skeleton (only the red area is counted), and N_d is the total number of pixels of the skeleton to be evaluated. The relationship among these parameters is clarified in a Venn diagram (Fig. 10). However, considering that all fracture skeletons are single pixel, in the process of binary image skeletonization, some pixels will shift inevitably. Therefore, an approximation method is used to estimate N_p: a reconstructed fracture network is obtained by dilating standard fracture skeleton with structural elements of 15 pixels; then, the pixels of the skeleton to be evaluated that fall in the fracture network are regarded as N_p.

3.2 The Influence of Shading Azimuth on the Results of Fracture Extraction

The altitude angle used for the cases is 45°. The 8 azimuths are divided into four groups with an angle difference of 180°, respectively, and stacked along the direction of 45°, 225°, 135°, 315°, 0°, 180°, 90°, 270° in order. The above-mentioned depth image processing method is applied and a shading image is added each time to obtain the fracture skeletons and calculate the PDR and ER. The results are shown in Fig. 11. When only the 45° depth image is used, the positive detection rate (PDR) of fracture extraction is low. Because the altitude for fractures of the rock sample surface is too large which results in insufficient shading of the fractures and leads to missed detection. As the number of fractures increases, the proportion of the fracture skeleton extracted from a single shading image will decrease. When the four fracture shading images are used together, i.e., the shading images at 45°, 225°, 135°, and 315°, the integrity of the fractures is close to the optimal solution. Nevertheless, adding more shading images will not effectively increase PDR, but waste computing resources. Particularly, as for rock sample 2, the PDR decreases when the 135°shading image is added. There are only two fractures in the image, and the long one has a large difference in height between the two sides, which results in deviations in the actual fractures. However, the error can be corrected by the subsequent superimposed shading images. It can be found from Fig. 11(b) that the error detection rate (ER) increases with the growing of number of depth images used. When 1–4 depth images were used, the error detection rate increased greatly, while the curve became flat after 4 images. In particular, for Case 1, since few fractures exist on the rock sample surface and there is almost no height difference between both sides of the fractures, its error detection rate is always 0. Therefore, only four depth images are processed in this paper.

3.3 Comparison with Fracture Extraction Results from Color Images

3.3.1 Color Image Processing Algorithm

The resolution of the generated depth image is 3000 × 3000 pixels. The color image taken by the Canon EOS 5D Mark IV camera is adjusted to the same resolution, since the pixels of the color image and the depth image are exactly matched, and the same pixels are used to represent the information of the same area.

Most color images of the rock surface have the following features: a large amount of information, rich gray levels, numerous noises, low contrast between information, and curvilinear fractures. In addition, most fracture pixels have small gray values. If the grayscale ranging from 0 to M ($M > 10$) are defined as the dark region of an image (M is the gray scale with the highest occurrences), the main fracture skeleton pixels are distributed in dark regions. Based on the above features, an automatic extraction algorithm of rock mass fracture, based on image dark region curvilinear structure enhancement (DRCSE), is proposed for data collection. In the image pre-processing stage, this algorithm mainly depends on the curvilinear structure enhancement filter Frangi et al. (2000). It uses the homomorphic filtering

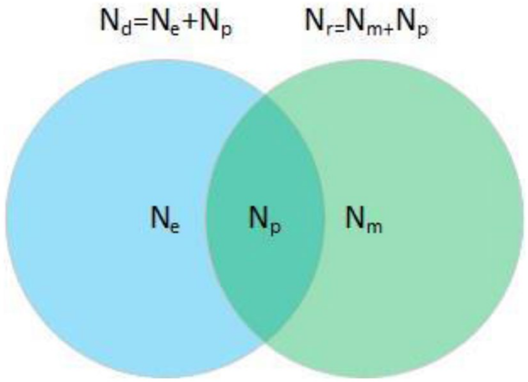

Fig. 10 Venn diagram of Np Ne, Nm, Nr and Nd

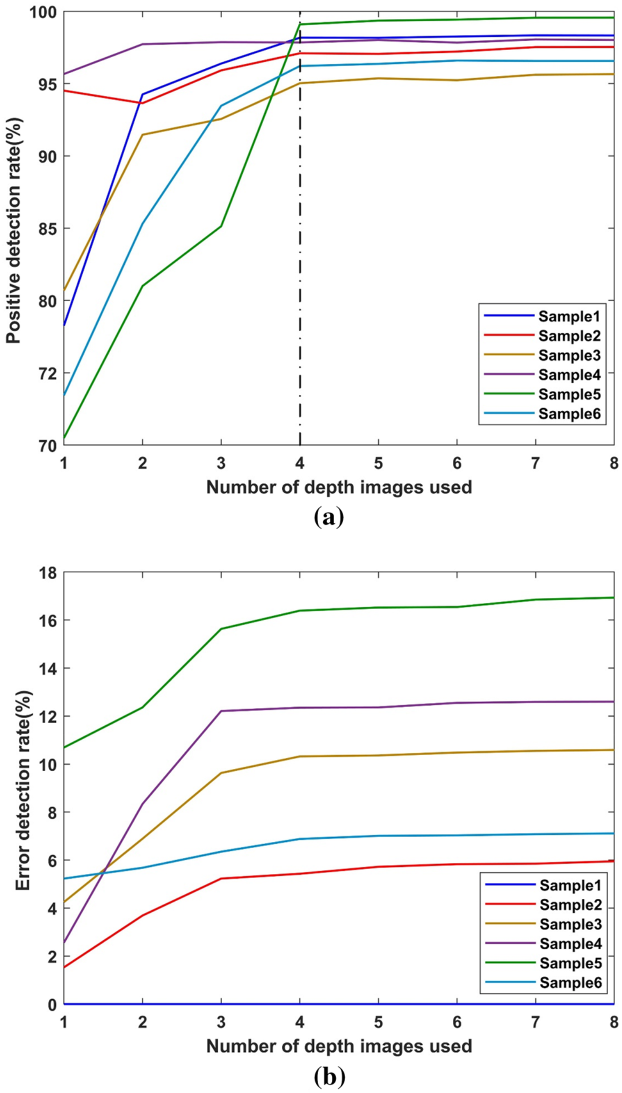

(a)

(b)

Fig. 11 The influence of adding depth images on the result of fracture extraction, **a** the relationship between the used depth images of all azimuths and PDR of the fracture skeleton, **b** the relationship between the used depth images of all azimuths and ER of the fracture skeleton

coupled with Gamma transforming to improve the contrast of dark regions with reduced noise. Thus, the fracture skeleton of the rock surface image could be accurately extracted through this method. Particularly, to obtain the most suitable value of Gamma transform parameter for different rock surface images to enhance dark regions contrast, a new edge-entropy (EE) index is proposed to describe the quality of the contrast-enhanced image. Particle swarm optimization is utilized to calculate the value of Gamma transforming parameters that maximize the EE index. The EE index is defined as follows (Tang et al. 2021):

$$EE = \ln(E(g(r,c))) \times H(g(r,c)), \tag{17}$$

where $g(r,c)$ is the image after Gamma transforming, $E()$ is the number of edge pixels detected by the Canny operator, and $H()$ is the one-dimensional gray entropy of the image.

In the image segmentation stage, the maximum entropy method is used to select a threshold automatically to binarize the image. Finally, the result of fracture skeleton extraction could be obtained by residual noise reduction through area thresholds, opening and closing operations to fill tiny holes, morphological skeleton extraction, and finally the skeleton burr removal.

3.3.2 Discussion

The fracture skeleton *PDR*, *ER* and *MR* recognized from the color image and depth image are shown in Table 2. The typical feature of sample 1 is the three mineral particles. Few fractures can be detected through image processing, and some reasons can account for this: the fracture width is extremely small, the fractures are hidden among various minerals, and the colors of both the fractures and mica are black. In comparison, the fracture skeleton extracted from

Table 2 PDR, ER and MR of rock samples

Rock sample	Image category	PDR	ER	MR
Rock sample 1	RGB	0.0697	2.0177	0.9290
	depth	**0.9817**	0.0000	0.0183
Rock sample 2	RGB	0.8323	0.8654	0.1677
	depth	**0.9709**	0.0543	0.0291
Rock sample 3	RGB	0.6163	5.1786	0.3837
	depth	**0.9502**	0.1032	0.0498
Rock sample 4	RGB	0.8926	3.1024	0.1074
	depth	**0.9784**	0.1235	0.0216
Rock sample 5	RGB	0.6810	0.9526	0.3190
	depth	**0.9909**	0.1639	0.0091
Rock sample 6	RGB	0.3109	0.8632	0.6891
	depth	**0.9621**	0.0688	0.0379

The significance of bold in the table is the emphasis on higher PDF of fractures extracted from depth images the depth image is almost noise-free with high fracture integrity, because the regions other than fractures in the rock sample is smooth, and the iterative median filtering is adopted for depth image processing. For all rock samples, the positive detection rate of depth images exceeds 95% and the average error rate is only 8.57%. The main source of error is skeleton burrs, which can be further optimized by burr removal algorithms if necessary.

The error rate of the fracture skeleton obtained from the color image is relatively high due to the following two reasons: (a) Non-curvilinear features are fragmentarily extracted and processed, which results in more noise. (b) Curvilinear features, such as the original cracks and the interstitial minerals, have also been detected and processed, but not been included in the standard fracture skeleton. The positive detection rate of the fracture skeleton obtained from the color image is generally low, with only rock samples 2 and 4 exceeding 80%, because these two rock samples have large fracture width, simple image information, high contrast between the features, and no influence from micro-cracks. Except for these two samples, abundant missed detections are found in other images.

For rock samples 2, 3, 4, if the color image skeleton and the depth image skeleton are fused and the skeleton source is represented by different colors, a classified fracture skeleton can be obtained. In the future numerical modelling process, specific material properties could be assigned to corresponding fracture skeletons, to make the numerical simulation results closer to reality.

3.4 Overall Performance of the Proposed Method

The main contribution of this method is to enhance the color image of the fractures using the depth image for the first time. Compared with the fracture extraction algorithm based only on the digital image, it has two distinct advantages:(a) The integrity and accuracy of the fracture skeleton are extensively improved, and color images can be supplemented to recognize broken or missed fractures; (b) Combined with the color image processing results, the pixel backtracking algorithm can distinguish curvilinear structures, which can provide a more accurate basis for subsequent numerical modeling and calculation.

Yet, several problems exist: (1) The recognition of existing features of rock samples can only be provided by color images, thus fractures and other curvilinear structures can only be distinguished when the fracture skeleton extracted from the color image is accurate. However, the DRCSE algorithm for color image processing is not reliable for images with intense information and extremely low contrast. (2) The rock samples used in this article are regular with smooth surfaces. Whereas for large-scale rock masses and other laboratory-scale rock samples, the fractures are more likely to exist on a rough surface. Thus, more noise and interference are unavoidable with this method. (3) When the generated depth image and the color image are simply registered, there will be an offset of about 10 pixels that cannot be detected by human eyes.

Hence, in the future, the fracture extraction method could be improved from two perspectives: enhancing the effect of the existing fracture extraction algorithm, and expanding the information sources. For color image processing algorithms, artificial intelligence related technologies can be introduced to enhance the robustness of image processing algorithms. For the depth image extraction algorithm, continuous improvement is required to develop the recognition of rock mass discontinuities at the engineering scale. In addition, proper integration of the two results worth more attention. Finally, other more accurate registration techniques need to be developed to adjust the pixel shift.

4 Conclusions

In this paper, a fracture extraction method for laboratory-scale rock samples is proposed using the image processing algorithms based on the point cloud. The disordered depth value of point cloud is obtained through the pose transformation of the rock sample model, and a high-precision and ordered preliminary depth image is then generated through the Kriging interpolation. Next, to clarify the fractures in the depth image, the rock sample is irradiated with parallel light from 4 angles through the hill shading method. Finally, according to the characteristics of the depth image histogram, an image processing algorithm is used to accurately extract the fractures. This method combines the advantages of clear fractures in point cloud data and mature image processing algorithms. The average accuracy of fracture recognition exceeds 95%, which provides a new idea for extracting fractures in various destructive experiments of rock, and may be further developed with deep learning for extracting the discontinuity features under typical engineering scale.

Acknowledgements This work was financially supported by the Innovative and Entrepreneurial Talented Program of Jiangsu Province and the National Natural Science Foundation of China (11402070)

Declarations

Conflict of interest The authors declare that they have no known competing financial interests or personal relationships that could have appeared to influence the work reported in this paper.

References

Achanta R, Shaji A, Smith K et al (2012) SLIC superpixels compared to state-of-the-art superpixel methods. IEEE Trans Pattern Anal Mach Intell 34:2274–2282. https://doi.org/10.1109/TPAMI.2012.120

Cong R, Lei J, Fu H et al (2020) Going from RGB to RGBD saliency: a depth-guided transformation model. IEEE Trans Cybern 50:3627–3639. https://doi.org/10.1109/TCYB.2019.2932005

Damien P, Nader RB, Yaacoub C, Lahoud J-C (2019) Iliopectineal Line Fracture Detection for Computer-Aided Acetabular Fracture Classification. 2019 Ninth Int. Conf. Image Process. Theory, Tools Appl. (IPTA), 1–5

Fernandes LAF, Oliveira MM (2008) Real-time line detection through an improved Hough transform voting scheme. Pattern Recognit 41:299–314

Frangi R, Niessen WJ, Vincken K, Viergever M (2000) Multiscale vessel enhancement filtering. Med Image Comput Comput Assist Interv 1496

Galdames FJ, Perez CA, Estévez PA, Adams M (2017) Classification of rock lithology by laser range 3D and color images. Int J Miner Process 160:47–57

Galdames FJ, Perez CA, Estévez PA, Adams M (2019) Rock lithological classification by hyperspectral, range 3D and color images. Chemom Intell Lab Syst 189:138–148

Gao W, Fu D, Li Y, Song Y (2019) An image edge detection method based on wavelet transform modulus maximum. Acta Microsc 28:1507–1515

He C, Wang W (2010) A PCNN-Based Edge Detection Algorithm for Rock Fracture Images. 2010 Symp. Photonics Optoelectron. Photonics Optoelectron. (SOPO), 2010 Symp. 1–4

Hu T, Wu T, He H (2011) Stereo matching-based low-textured scene reconstruction for ALV navigation. 2011 Int. Conf. Image Anal. Signal Process. (IASP), 204–209

IAroslavskii LP (2013) Theoretical foundations of digital imaging using MATLAB. CRC Press

Janoch A, Karayev S, Jia Y, et al (2011) A category-level 3-D object dataset: Putting the Kinect to work. 2011 IEEE Int. Conf. Comput. Vis. Work. (ICCV), 1168–1174

Javed A (2020) Experimental investigation of propeller induced flow on flying wing micro aerial vehicle for improved 6DOF modeling. IEEE Access 8:179626–179647. https://doi.org/10.1109/ACCESS.2020.3026005

Ju Y, Xi C, Zhang Y et al (2018) Laboratory in situ CT observation of the evolution of 3D fracture networks in coal subjected to confining pressures and axial compressive loads: a novel approach. Rock Mech Rock Eng 51:3361. https://doi.org/10.1007/s00603-018-1459-4

Kumar A, Sodhi SS (2020) Comparative Analysis of Gaussian Filter, Median Filter and Denoise Autoenocoder. 2020 7th Int. Conf. Comput. Sustain. Glob. Dev. (INDIACom), 45–51

Lempitsky V, Kohli P, Rother C, Sharp T (2009) Image segmentation with a bounding box prior. 2009 IEEE 12th Int. Conf. Comput. Vision, Comput. Vision, 277–284

Lemy F, Hadjigeorgiou J (2004) A digital face mapping case study in an underground hard rock mine. Can Geotech J 41:1011–1025

Li Q, Zou Q, Zhang D, Mao Q (2011) FoSA: F* Seed-growing approach for crack-line detection from pavement images. Image Vis Comput 29:861–872

Li J, Li N, Li H, Zhao J (2017a) An SHPB test study on wave propagation across rock masses with different contact area ratios of joint. Int J Impact Eng 105:109–116

Li L, Yang F, Zhu H et al (2017b) An improved RANSAC for 3D point cloud plane segmentation based on normal distribution transformation cells. Remote Sens 9:433

Li J, Rong L, Li H, Hong S (2019) An SHPB test study on stress wave energy attenuation in jointed rock masses. Rock Mech Rock Eng 52(2):403–420

Liang Y (2016) Rock fracture skeleton tracing by image processing and quantitative analysis by geometry features. J Geophys Eng 13:273–284. https://doi.org/10.1088/1742-2132/13/3/273

Liu L, Xiao J, Wang Y (2019) Major orientation estimation-based rock surface extraction for 3D rock-mass point clouds. Remote Sens 11:635. https://doi.org/10.3390/rs11060635

Lu G, Zhou J, Li Y, et al (2020) The influence of minerals on the mechanism of microwave-induced fracturing of rocks. J Appl Geophys 180

Matheron G (1963) Principles of geostatistics. Econ Geol 58:1246–1266

Otsu N (1979) A threshold selection method from gray-level histograms. IEEE Trans Syst Man Cybern 9:62–66. https://doi.org/10.1109/TSMC.1979.4310076

Pei Y, Liu C, Lou R (2020) Multi-scale edge detection method for potential field data based on two-dimensional variation mode decomposition and mathematical morphology. In: IEEE access VO - 8. IEEE, United States, p 161138

Qian RJ, Huang TS (1996) Optimal edge detection in two-dimensional images. IEEE Trans Image Process 5:1215–1220. https://doi.org/10.1109/83.502412

Silberman N, Hoiem D, Kohli P, Fergus R (2012) Indoor Segmentation and Support Inference from RGBD Images BT—Computer Vision – ECCV 2012. In: Fitzgibbon A, Lazebnik S, Perona P, et al. (eds). Springer Berlin Heidelberg, Berlin, Heidelberg, pp 746–760

Sivakugan N, Shukla SK, Das BM (2013) Rock mechanics : An Introduction. Taylor & Francis

Talab AMA, Huang Z, Xi F, HaiMing L (2016) Detection crack in image using Otsu method and multiple filtering in image processing techniques. Opt Int J Light Electron Opt 127:1030–1033

Tan X, Konietzky H, Chen W (2016) Numerical simulation of heterogeneous rock using discrete element model based on digital image processing. Rock Mech Rock Eng 49:4957. https://doi.org/10.1007/s00603-016-1030-0

Tang Y, He L, Lu W et al (2021) A novel approach for fracture skeleton extraction from rock surface images. Int J Rock Mech Min Sci 142:104732. https://doi.org/10.1016/j.ijrmms.2021.104732

Umili G, Ferrero A, Einstein H (2013) new method for automatic discontinuity traces sampling on rock mass 3D model. Comput Geosci 51:182–192. https://doi.org/10.1016/j.cageo.2012.07.026

Wang X (1992) Adaptive multistage median filter. Signal Process IEEE Trans 40:1015–1017. https://doi.org/10.1109/78.127983

Wang F, Xiao J, Wang Y (2019) Efficient rock-mass point cloud registration using n -point complete graphs. IEEE Trans Geosci Remote Sens 57:9332–9343. https://doi.org/10.1109/TGRS.2019.2926201

Wang S, Liang S, Peng F, Zhang W (2020) Image edge detection algorithm based on fuzzy set. J Intell Fuzzy Syst 38:3557–3566

Xiao J, Owens A, Torralba A (2013) SUN3D: A Database of Big Spaces Reconstructed Using SfM and Object Labels. In: 2013 IEEE Int. Conf. Comput. Vision, Comput. Vis. (ICCV), 1625–1632

Xiao H, He L, Li X et al (2020) Texture synthesis: a novel method for generating digital models with heterogeneous diversity of rock materials and its CGM verification. Comput Geotech. https://doi.org/10.1016/j.compgeo.2020.103895

Xu W, Zhang Y, Li X et al (2020) Extraction and statistics of discontinuity orientation and trace length from typical fractured rock mass: A case study of the Xinchang underground research laboratory site. China, Eng Geol, p 269

Xu T, He L, Zheng Y et al (2021) Experimental and numerical investigations of microwave-induced damage and fracture formation in rock. J Therm Stresses 43(13):1487–1512. https://doi.org/10.1080/01495739.2020.1865857

Yang X, Li M, Na J, Liu K (2017) Gully boundary extraction based on multidirectional hill-shading from high-resolution DEMs. Trans GIS 21:1204–1216

Yi X, Zhang R, Li H, Chen Y(2019) An MFF-SLIC hybrid superpixel segmentation method with multi-source RS data for rock surface extraction. Appl Sci 9

Zhang P, Du K, Tannant DD et al (2018) Automated method for extracting and analysing the rock discontinuities from point clouds based on digital surface model of rock mass. Eng Geol 239:109–118

Zhang P, Zhao Q, Tannant DD et al (2019a) 3D mapping of discontinuity traces using fusion of point cloud and image data. Bull Eng Geol Environ Off J IAEG 78:2789. https://doi.org/10.1007/s10064-018-1280-z

Zhang Y, Zhao T, Yin Y, et al (2019b) Numerical research on energy evolution in granite under different confining pressures using otsu's digital image processing and PFC2D. SYMMETRY-BASEL 11

Zhao QH, Zhao XB, Zheng YL, et al (2020) Heating characteristics of igneous rock-forming minerals under microwave irradiation. Int J Rock Mech Min Sci 135

Zhu Z, German S, Brilakis I (2011) Visual retrieval of concrete crack properties for automated post-earthquake structural safety evaluation. Autom Constr 20:874–883

Zou Y, Li J, Zhao J (2019) A novel experimental method to investigate the seismic response of rock joints under obliquely incident wave. Rock Mech Rock Eng 52(9):3459–3466